Large and Reversible Strain-Tunable Valley Polarization in Two-Dimensional Altermagnetic Zr-Based Oxyhalide Monolayers

Ning-Ning Zhao[1,†], Jing-Jing Zhang[1,†], Xiao-Yao Hou[2], Xiu-Li Yang[1], Shu-Feng Zhang[1,*], and Ping Li[1,*]

[1]School of Physics and Technology, University of Jinan, Jinan 250022, China
[2]School of Physics and Engineering, Henan University of Science and Technology, Luoyang 471023, China

[†]These authors contributed equally to this work.
[*]Corresponding authors: sps_zhangsf@ujn.edu.cn; ss_lip@ujn.edu.cn.

Abstract: Altermagnets combine compensated magnetic order with momentum-dependent spin splitting, providing a promising platform for spin–valley control without net magnetization. Here, using first-principles calculations, we identify monolayer Zr_2Cl_2O, Zr_2Br_2O, and Janus Zr_2ClBrO as dynamically stable altermagnetic semiconductors that retain their structural frameworks in 300 K AIMD simulations. The X and Y valleys are dominated by Zr 4*d* orbitals and carry opposite spin polarizations in the nonrelativistic limit. Uniaxial strain shifts the two valleys in opposite directions, enabling reversible control of both the magnitude and sign of the valley polarization. Under only $\pm 2\%$ uniaxial strains, the valence-band valley splittings reach 192–212 meV in Zr_2Cl_2O and Zr_2Br_2O and 84.4–158.8 meV in Zr_2ClBrO. Moreover, rotating the strain axis by 90° reverses the valley ordering. In addition, stronger compression closes the band gap and induces an inversion between opposite-spin bands, while the crossing opens a small gap with SOC. These results establish Zr-based oxyhalide monolayers as promising candidates for mechanically tunable altermagnetic valleytronics.

Keywords: altermagnetism; valley polarization; two-dimensional materials; strain engineering
PACS: 75.50.Ee; 71.70.Fk; 73.22.-f; 71.15.Mb

1. Introduction

Altermagnetism has recently emerged as a distinct class of collinear magnetism that combines a fully compensated magnetic configuration in real space with pronounced spin splitting in momentum space. [1–5] Unlike conventional collinear antiferromagnets, whose opposite-spin sublattices are typically related by inversion or translation and therefore often retain spin-degenerate bands, the magnetic sublattices of an altermagnet are connected by crystal rotations or mirror operations. This unconventional symmetry relation produces alternating momentum-dependent spin polarizations with characteristic *d*-, *g*-, or *i*-wave forms while preserving a vanishing net magnetization. [6–8] Altermagnets therefore combine the negligible stray fields and potentially fast dynamics of antiferromagnets with the spin-polarized electronic structures usually associated with ferromagnets, offering a promising platform for spin-dependent transport and information processing. [9–12]

Valleytronics exploits inequivalent extrema in electronic band structures as an additional degree of freedom for information encoding and transport. [13, 14] In conventional two-dimensional valley materials, such as gapped graphene and transition-metal dichalcogenide monolayers, the K and K' valleys are related by time-reversal symmetry and are consequently degenerate. [15–17] A finite valley polarization therefore generally requires an external magnetic field, magnetic proximity coupling, or magnetic doping. [18–20] Two-dimensional altermagnets provide a different route to valley manipulation. [21–27] In tetragonal altermagnets, the relevant valleys may occur at the time-reversal-invariant X and Y points and be connected by a combined spin–crystal symmetry rather than by time reversal. The two valleys can consequently carry opposite spin polarizations in the nonrelativistic limit. An in-plane anisotropic perturbation, particularly uniaxial strain, can shift the X- and Y-valley edges in opposite directions. The resulting strain-induced splitting is commonly termed the piezovalley effect and enables mechanical control of both the magnitude and sign of valley polarization. [21, 24]

Recent theoretical studies have demonstrated that strain engineering is an effective strategy for controlling valley polarization in two-dimensional altermagnets, including V_2Te_2O-derived oxychalcogenides, Nb_2Se_2O and Janus Nb_2SeTeO, V_2SeTeO, Ti_2Se_2S, Cr_2S_2, Cr_2SeO, Janus Cr_2SO, and V_2AsBrO. [28–37] However, two-dimensional material platforms that simultaneously exhibit a robust altermagnetic ground state, large and reversible valley splitting, and pronounced strain-induced band reconstruction remain scarce.

In this work, based on first-principles calculations, we investigate the structural stability, magnetic order, electronic properties, and strain response of the Zr-based oxyhalide monolayers Zr_2Cl_2O, Zr_2Br_2O, and Janus Zr_2ClBrO. The altermagnetic ground state of Zr_2Cl_2O is shown to remain stable against competing nonmagnetic, ferromagnetic, stripe, and zigzag orders. All three monolayers are dynamically stable altermagnetic semiconductors and retain their structural frameworks in 300 K AIMD simulations. Uniaxial strain reversibly switches the valley ordering and produces valley polarization approaching 0.2 eV in Zr_2Cl_2O and Zr_2Br_2O. These results establish Zr-based oxyhalides as promising candidates for mechanically controlled altermagnetic valleytronics.

2. Computational methods

Our first-principles calculations were performed within density functional theory using the projector augmented-wave method as implemented in the Vienna *Ab initio* Simulation Package. [38–40] The Perdew–Burke–Ernzerhof generalized-gradient approximation was adopted for exchange and correlation. [41] The plane-wave cutoff energy was 520 eV, and the Brillouin zone was sampled using a $16 \times 16 \times 1$ k-point mesh. A vacuum layer larger than 15 Å was introduced to suppress interactions between periodic images. The electronic convergence threshold was 10^{-6} eV, and the structures were relaxed until the residual force on each atom was below 0.01 eV/Å. The Zr 4*d* states were treated within the GGA+U with $U_{\mathrm{eff}} = 4.0$ eV in the main calculations [42–44]. Phonon dispersions were calculated using the finite-displacement method in a $4 \times 4 \times 1$

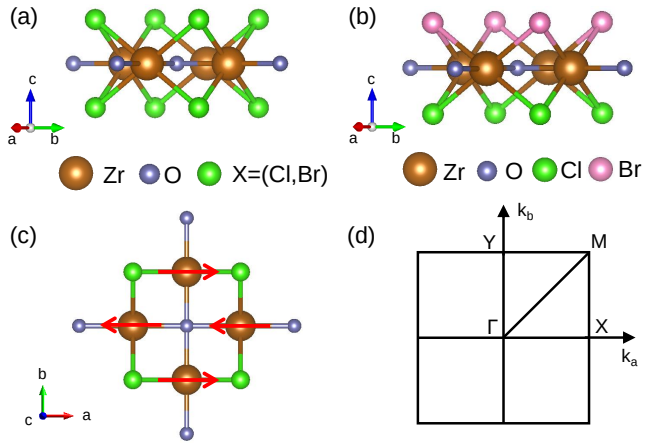


Figure 1. Side views of (a) Zr_2X_2O ($X = Cl, Br$) and (b) Janus Zr_2ClBrO. (c) Top view of the altermagnetic configuration; the red arrows indicate the Zr magnetic moments. (d) Two-dimensional Brillouin zone with the high-symmetry points labeled.

supercell with the PHONOPY code [45]. *Ab initio* molecular dynamics simulations were carried out for 10 ps at 300 K in a $3 \times 3 \times 1$ supercell with a 1 fs time step. [46] The spin-projected band structures were calculated using WANNIER90 software [47,48], where a tight-binding Hamiltonian was constructed using maximally localized Wannier functions for the outermost *s*, *p*, and *d* orbitals of Zr and the outermost *s* and *p* orbitals of O, Cl, and Br atoms.

3. Results and discussion

3.1. Crystal structure and magnetic ground state

The Zr-based oxyhalide monolayers Zr_2Cl_2O and Zr_2Br_2O are isostructural with the previously proposed V_2Te_2O monolayer and crystallize in the tetragonal $P4/mmm$ space group (No. 123). [28,49] Each monolayer consists of a central Zr–O layer sandwiched between two chemically equivalent halogen layers [Fig. 1(a)]. Each Zr atom is coordinated by four halogen atoms and two O atoms, forming a distorted octahedral environment. Janus Zr_2ClBrO is obtained by replacing one Cl layer of Zr_2Cl_2O with Br [Fig. 1(b)]. This substitution breaks inversion and the out-of-plane mirror symmetry, reducing the space group to $P4mm$ (No. 99) while preserving the in-plane square lattice. The optimized lattice constants are $a = b = 4.483$ Å for Zr_2Cl_2O, 4.504 Å for Zr_2Br_2O, and 4.487 Å for Zr_2ClBrO. Figure 1(c) shows the top view of the collinear AM configuration, in which antiparallel Zr moments form two compensated magnetic sublattices. The corresponding two-dimensional Brillouin zone and the high-symmetry points are shown in Fig. 1(d).

The magnetic ground state was determined by comparing the AM, zigzag, stripe, FM, and NM configurations. Representative magnetic structures for Zr_2Cl_2O are shown in Figs. 2(a)–2(d). Figure 2(e) presents the relative energies $\Delta E_i = E_i - E_{AM}$ per unit cell as a function of U_{eff} over the range 0–5 eV. The energies of all competing states are higher than that of the AM state throughout this range, and increasing U_{eff} generally enlarges the energy separation between them. The apparent kink in the FM curve near $U_{eff} = 2$ eV coincides with the onset of finite local Zr moments. At $U_{eff} = 4.0$ eV, the relative energies of the competing magnetic configurations for all three monolayers are positive (Table S1 of the supplementary material), confirming the AM ground state among the configurations considered. Guided by the reported Zr-*d* interaction parameters by Moore *et al.*, [44], we adopt U_{eff} =4.0 eV, which yields local Zr moments of 1.002 μ_B, 0.973 μ_B, and 0.976 μ_B for Zr_2Cl_2O, Zr_2Br_2O, and Zr_2ClBrO, respectively. Furthermore, magnetic anisotropy energy (MAE) calculations reveal that the Néel vector favors the crystallographic *x* direction, as illustrated in Fig. 1(c).

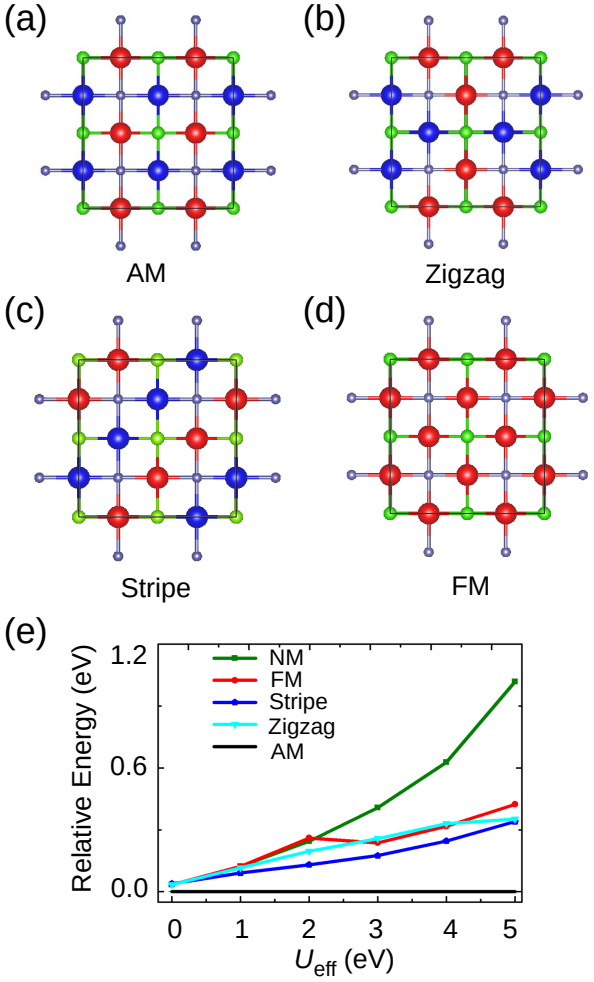


Figure 2. (a) Altermagnetic (AM), (b) zigzag antiferromagnetic, (c) stripe antiferromagnetic, and (d) ferromagnetic (FM) configurations in a $2 \times 2 \times 1$ supercell. Red and blue Zr spheres denote opposite spin orientations. (e) Relative energies per unit cell of the NM, FM, stripe, and zigzag states with respect to the AM state as functions of U_{eff}. The AM energy is set to zero at each U_{eff}.

Figure 3 presents the phonon dispersion and *ab initio* molecular dynamics results. The calculated phonon spectra contain no imaginary-frequency modes, confirming the dynamical stability of all three monolayers. During the 10 ps simulations at 300 K, the total energies fluctuate around stable mean values without systematic drift, and the final configurations retain their layered frameworks without bond breaking or irreversible reconstruction. These 300 K AIMD simulations demonstrate the finite-temperature structural stability of all three monolayers.

3.2. Electronic structure and altermagnetic valley states

After establishing its magnetic ground state and structural stability, we investigate the electronic properties of the three monolayers. As shown in Figs. 4(a)–4(c), the spin-resolved band structures calculated without SOC show that all three systems are altermagnetic semiconductors with pronounced

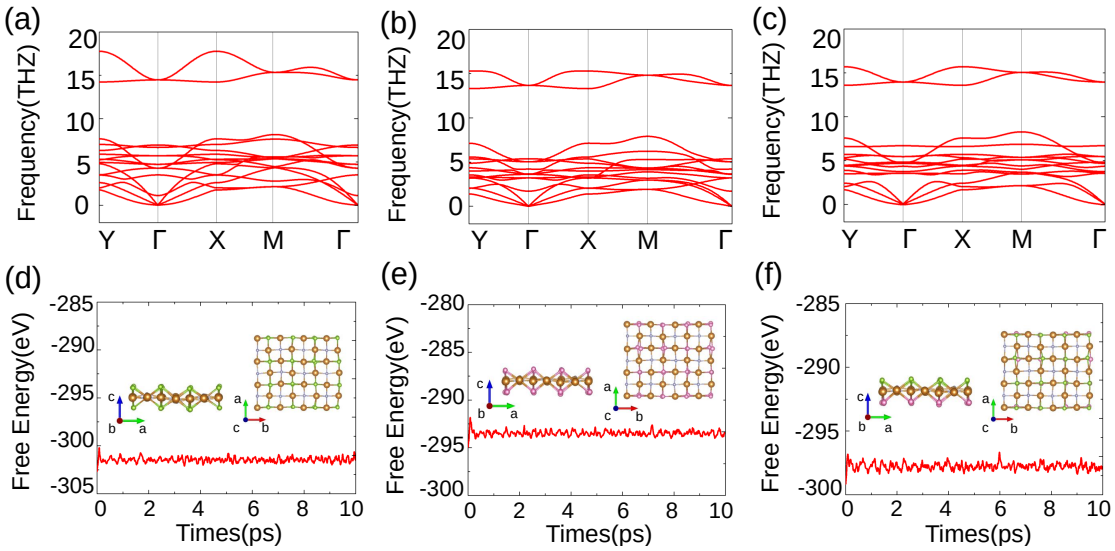


Figure 3. Phonon dispersions of (a) Zr_2Cl_2O, (b) Zr_2Br_2O, and (c) Zr_2ClBrO, respectively. Total-energy evolution of (d) Zr_2Cl_2O, (e) Zr_2Br_2O, and (f) Zr_2ClBrO during molecular dynamics simulations at 300 K; the insets show representative final structures.

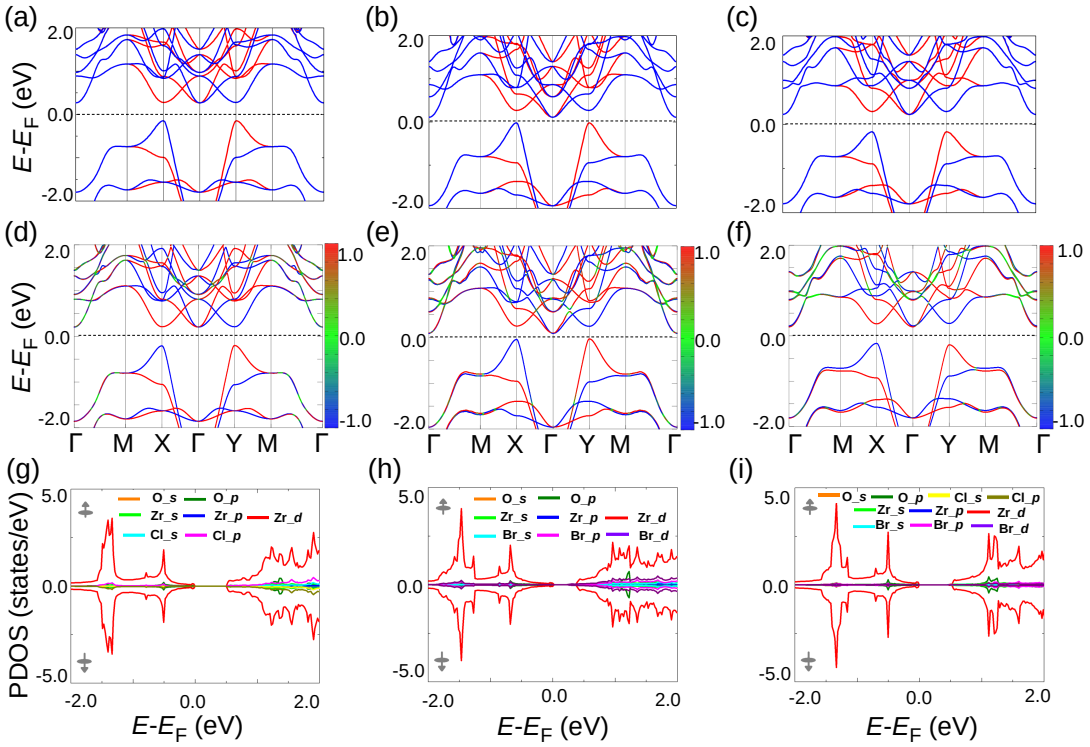


Figure 4. Band structures of (a) Zr_2Cl_2O, (b) Zr_2Br_2O, and (c) Janus Zr_2ClBrO calculated without SOC. Red and blue denote the two spin channels. Band structures calculated with SOC of (d) Zr_2Cl_2O, (e) Zr_2Br_2O, and (f) Janus Zr_2ClBrO colored by the expectation value of the spin projection. Orbital-projected densities of states (DOS) calculated without SOC of (g) Zr_2Cl_2O, (h) Zr_2Br_2O, and (i) Janus Zr_2ClBrO.

momentum-dependent spin splitting. The X and Y valleys are connected by the spin-group operation $\{C_2^{\perp} \parallel M_{110}\}$: the diagonal mirror M_{110} exchanges X and Y, while the accompanying 180° spin rotation reverses the spin polarization. Consequently, the two valleys are degenerate but carry opposite spins. The momentum-dependent spin splitting and opposite spin characters of the X and Y valleys persist over the investigated range $2.0 \leq U_{\mathrm{eff}} \leq 5.0$ eV (see Fig. S1 of the supplementary material), demonstrating that the qualitative altermagnetic valley features are robust against moderate variations in U_{eff}.

Upon inclusion of SOC, the spin and lattice degrees of freedom become locked, and the symmetry is described by the magnetic group of the x-oriented Néel state. For centrosymmetric Zr_2Cl_2O and Zr_2Br_2O, the symmetry is reduced from $P4/mmm$ to the type-III magnetic space group $Pm'm'm$ (No. 47.252). For Janus Zr_2ClBrO, the absence of inversion and the out-of-plane mirror symmetry gives $Pm'm2'$ (No. 25.59). Neither magnetic group contains an operation that exchanges k_x and k_y within a fixed magnetic domain; hence, a finite intrinsic X–Y splitting is symmetry allowed. At zero strain, the SOC-induced valley splittings $\Delta E_v = E_v(X) - E_v(Y)$ are -4.69, -12.65, and $+32.25$ meV for Zr_2Cl_2O, Zr_2Br_2O, and Zr_2ClBrO, respectively. Nevertheless, the nonrelativistic altermagnetic exchange remains dominant, and the X and Y

valleys retain opposite leading spin projections [Figs. 4(d)–4(f)]. The X and Y valleys retain opposite dominant spin projections after SOC is included, indicating a robust coupling between the spin and valley degrees of freedom. The calculated partial densities of states in Figs. 4(g)–4(i) show that the states near the Fermi level are dominated by 4*d* orbitals of Zr atoms.

3.3. Strain-tunable valley polarization

To explore the strain tunability of the valley states, we next examine the evolution of the SOC band structure under uniaxial deformation. The uniaxial strain along the i direction ($i = a, b$) is defined as $\varepsilon_i = (l_i - l_{i,0})/l_{i,0} \times 100\%$, where $l_{i,0}$ and l_i are the equilibrium and strained lattice constants along the strain direction, respectively. For strain applied along a (b), the perpendicular lattice constant b (a) is fixed at its equilibrium value, while all internal atomic coordinates are fully relaxed at each strain value. Figure 5 presents the calculated band structures of Zr_2Cl_2O under tensile and compressive strains applied along the a direction. Tensile strain raises the Y-valley valence-band edge relative to X, driving $\Delta E_v = E_v(X) - E_v(Y)$ to negative values, whereas compressive strain reverses the valley ordering and the sign of ΔE_v. The fundamental band gap decreases under both tensile and compressive strain. Upon further compression, the two bands belonging to opposite spin channels exchange their energy ordering, indicating a strain-induced band inversion [Fig. S2]. When SOC is included, the coupling between the two bands removes the crossing and opens a small anticrossing gap [Figs. 5(f)]. The corresponding SOC band structures of Zr_2Br_2O and Janus Zr_2ClBrO under uniaxial strain along the a and b directions are presented in Figs. S3–S6 of the supplementary material. These results confirm that rotating the strain axis by 90° reverses the relative ordering of the X and Y valleys in both systems.

The resulting strain dependences of the band gaps and valence-band valley polarizations for all three monolayers are summarized in Fig. 6. Under compressive strain , the band gaps of Zr_2Cl_2O [Fig.6(a)] and Zr_2Br_2O [Fig.6(b)] decrease as the magnitude of applied strain increases, while the band gap of Zr_2ClBrO [Fig.6(c)] first decreases and then increases with increasing compressive strain. This non-monotonic behavior results from the different nonlinear strain responses of the X-point valence-band edge and the Γ-point conduction-band edge. The inequivalent Cl and Br environments in the Janus structure may further enhance their different strain sensitivities. Although the three monolayers display different band-gap responses, their X-valley and Y-valley edges are highly sensitive to the strain direction. The valley-polarization panels show the total signed splitting, including both the intrinsic SOC contribution at zero strain and its strain-induced modification. Strains along a and b generate valley polarizations of opposite signs because rotating the strain direction by 90° reverses the relative ordering of X and Y. Thus, both the magnitude and sign of the valley polarization can be controlled reversibly. For Zr_2Cl_2O [Fig.6(d)]and Zr_2Br_2O [Fig.6(e)], ΔE_v varies nearly linearly over most of the investigated range, whereas Janus Zr_2ClBrO [Fig.6(f)]shows a more asymmetric response because of its chemically inequivalent Cl- and Br-terminated surfaces.

To place the piezovalley response of the Zr-based oxyhalides in the context of previously reported two-dimensional altermagnets, representative strain-induced valley splittings are summarized in Table 1. Under only ±2% uniaxial strain, Zr_2Cl_2O and Zr_2Br_2O exhibit valence-band splittings of approximately 192–212 meV, which exceed those reported for several V-based oxychalcogenides and are comparable in magnitude to the larger responses obtained in Nb_2Se_2O and Ti_2Se_2S under stronger deformation. Moreover, rotating the strain direction from a to b reverses the sign of the valley polarization, providing reversible control of the X–Y valley ordering without changing the magnetic configuration. In addition, Janus Zr_2ClBrO also exhibits sizable values of 84.4 and 158.8 meV, comparable to representative Janus altermagnets.

Table 1. Representative strain-induced valley polarizations in two-dimensional altermagnets. Absolute values are listed because the sign depends on the definition of valley polarization and the strain direction.

Material	Strain	valley polarization (meV)
Fe_2WSe_4/Fe_2WS_4 [22]	$-2\%/+2\%$	$\sim 10/\sim 15$
Nb_2Se_2O [30]	-3.44%	264.076
Ti_2Se_2S [33]	-4%	305.28
V_2Te_2O, V_2S_2O [28]	$-2\%/+2\%$	$\sim 50/\sim 60$
Zr_2Cl_2O (this work)	$-2\%/+2\%$	212/197.4
Zr_2Br_2O (this work)	$-2\%/+2\%$	209/192.3
V_2STeO, V_2SSeO [28]	$-2\%/+2\%$	$\sim 50/\sim 60$
V_2SeTeO [32]	$+4\%$	128
Cr_2SeO [35]	-4%	90
V_2AsBrO [37]	$+2\%$	161.9
Nb_2SeTeO [30]	-4%	21.10
Zr_2ClBrO (this work)	$-2\%/+2\%$	84.4/158.8

4. Conclusion

In summary, our first-principles calculations identify monolayer Zr_2Cl_2O, Zr_2Br_2O, and Janus Zr_2ClBrO as dynamically stable altermagnetic semiconductors with finite-temperature structural stability at 300 K. A comprehensive comparison of competing magnetic states shows that the compensated altermagnetic configuration remains the ground state for Zr_2Cl_2O throughout $U_{\text{eff}} = 0$–5 eV, confirming that the magnetic order is robust and not created by the Hubbard correction. The Zr 4*d*-dominated X and Y valleys carry opposite spin polarizations in the nonrelativistic limit. The coexistence of momentum-dependent spin splitting and vanishing net magnetization provides altermagnets with a distinct advantage for valley control, enabling coupled spin–valley manipulation without macroscopic stray fields or an external magnetic field. Uniaxial strain enables reversible control of their energy ordering, with valley splittings approaching 0.2 eV in Zr_2Cl_2O and Zr_2Br_2O. In addition, compressive strain substantially reconstructs the low-energy electronic structure, producing gap closure and band inversion between the opposite-spin channels in the nonrelativistic limit, followed by SOC-induced gap reopening. These properties make Zr-based oxyhalide monolayers promising platforms for mechanically controlled altermagnetic valleytronics with negligible net magnetization and reversible spin–valley control.

Supplementary material

See the supplementary material for the relative energies of competing magnetic configurations for all three monolayers at $U_{\text{eff}} = 4.0$ eV, the U_{eff}-dependent nonrelativistic band structures of Zr_2Cl_2O, the spin-resolved non-SOC band structures of Zr_2Cl_2O under -5% uniaxial and biaxial strains, and the

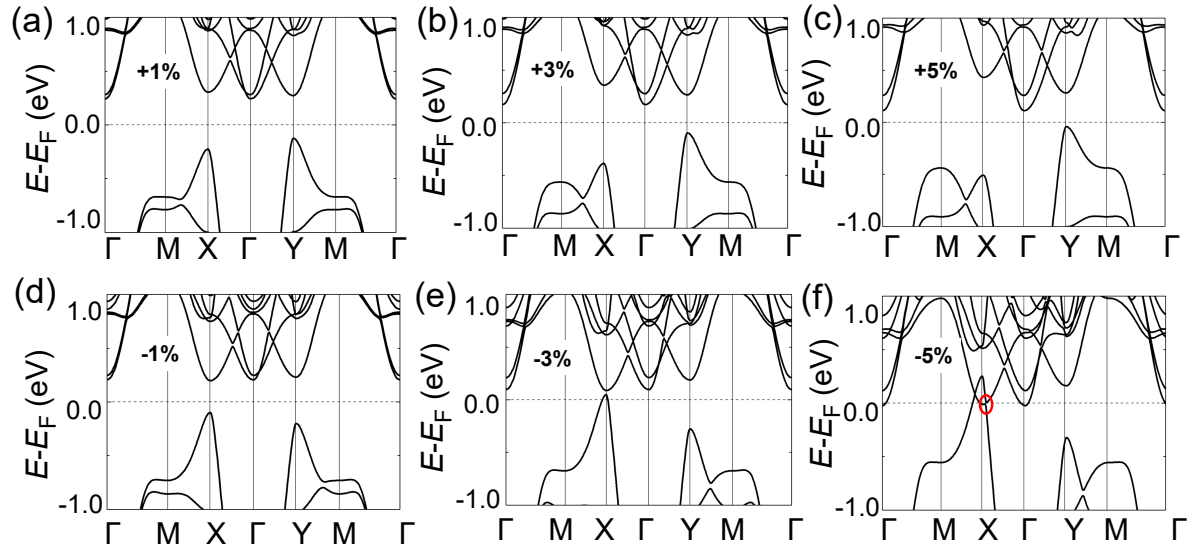


Figure 5. Band structures calculated with SOC of monolayer Zr_2Cl_2O under uniaxial (a)–(c) 1%, 3%, and 5% tensile strain and (d)–(f) −1%, −3%, and −5% compressive strain along the *a* axis.

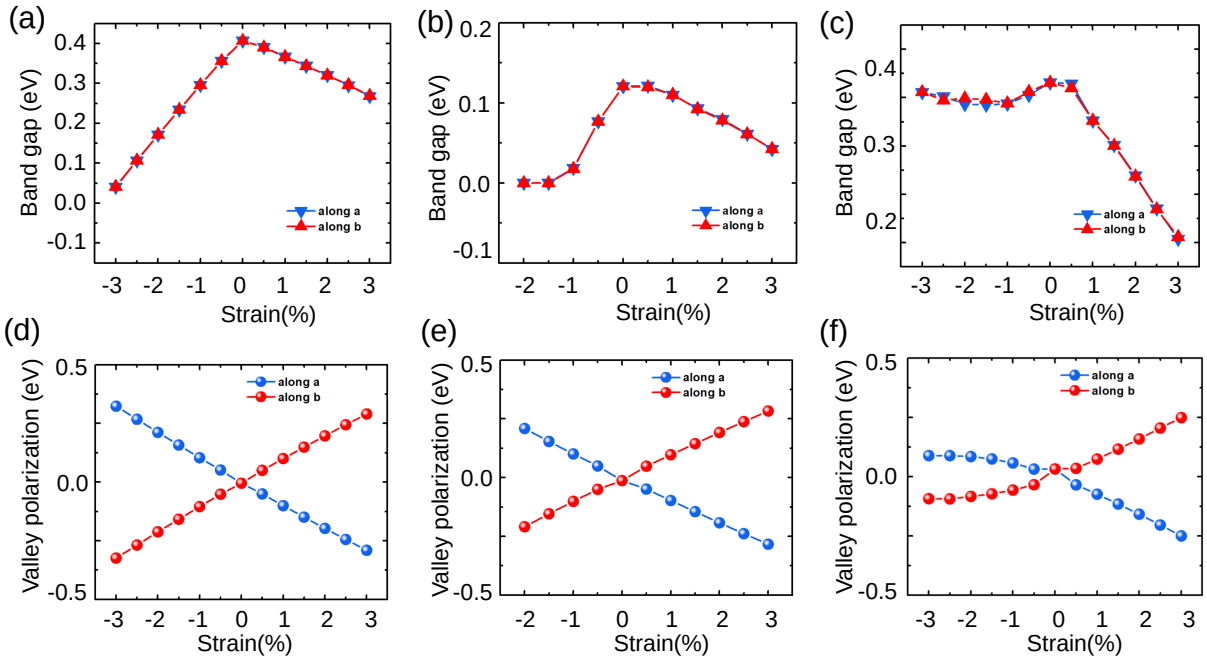


Figure 6. Band gaps and valence-band valley polarizations of (a) and (d) Zr_2Cl_2O, (b) and (e) Zr_2Br_2O, and (c) and (f) Zr_2ClBrO under uniaxial strain applied along the *a* and *b* directions. The valley polarization is defined as $\Delta E_v = E_v(X) - E_v(Y)$. The band gap is defined as $E_g = E_{CBM} - E_{VBM}$, where E_{CBM} and E_{VBM} denote the minimum conduction-band energy and maximum valence-band energy, respectively. Positive and negative strain values denote tensile and compressive strain, respectively.

SOC band structures of Zr_2Br_2O and Janus Zr_2ClBrO under uniaxial strain applied along the *a* and *b* directions.

Data availability

The data that support the findings of this study are available from the corresponding author upon reasonable request.

Acknowledgments

This work was supported by the National Natural Science Foundation of China (Grant No. 12404183), the Shandong Provincial Natural Science Foundation (Grant Nos. ZR2024QA014 and ZR2024QA137), the Higher Education Youth Innovation Science and Technology Support Program of Shandong Province (2025KJG021) and the University of Jinan Doctoral Fund Project (Grant Nos. XBS2476 and XBS2475). The numerical calculations were supported by the high-performance computing platform at the University of Jinan.

Conflict of interest

The authors have no conflicts to disclose.

References

[1] Šmejkal L, Sinova J and Jungwirth T 2022 *Phys. Rev. X* **12** 031042

[2] Šmejkal L, Sinova J and Jungwirth T 2022 *Phys. Rev. X* **12** 040501

[3] Krempaský J, Šmejkal L, D'Souza S W, Hajlaoui M, Springholz

G, Uhlířová K, Alarab F, Constantinou P C, Strocov V, Usanov D, Pudelko W R, González-Hernández R, Birk Hellenes A, Jansa Z, Reichlová H, Šobáň Z, Gonzalez Betancourt R D, Wadley P, Sinova J, Kriegner D, Minář J, Dil J H and Jungwirth T 2024 *Nature* **626** 517

[4] Fedchenko O, Minář J, Akashdeep A, D'Souza S W, Vasilyev D, Tkach O, Odenbreit L, Nguyen Q, Kutnyakhov D, Wind N, Wenthaus L, Scholz M, Rossnagel K, Hoesch M, Aeschlimann M, Stadtmüller B, Kläui M, Schönhense G, Jungwirth T, Birk Hellenes A, Jakob G, Šmejkal L, Sinova J and Elmers H J 2024 *Sci. Adv.* **10** eadj4883

[5] Lee S, Lee S, Jung S, Jung J, Kim D, Lee Y, Seok B, Kim J, Park B G, Šmejkal L, Kang C J and Kim C 2024 *Phys. Rev. Lett.* **132** 036702

[6] Hayami S, Yanagi Y and Kusunose H 2019 *J. Phys. Soc. Jpn.* **88** 123702

[7] Yuan L D, Wang Z, Luo J W, Rashba E I and Zunger A 2020 *Phys. Rev. B* **102** 014422

[8] Šmejkal L, González-Hernández R, Jungwirth T and Sinova J 2020 *Sci. Adv.* **6** eaaz8809

[9] Shi H, Jiang Y, Tian Y, Wang W, Li S, Gong W J and Kong X 2026 *Appl. Phys. Lett.* **128** 063101

[10] Chen Z, Zhan F, Qin Z, Ma D S, Xu D H and Wang R 2026 *Nano Lett.* **26** 4197

[11] Wang F, Zhang Y, Yang W, Zhang H and Xu X 2024 *Chin. Phys. B* **33** 017306

[12] Zhang X, Liu J, Huang W, Zhang F, Zhu M Y, Zhu Y P, Chen C, Liu C, Kim C and Shen D 2026 *Chin. Phys. Lett.* **43** 050709

[13] Schaibley J R, Yu H, Clark G, Rivera P, Ross J S, Seyler K L, Yao W and Xu X 2016 *Nat. Rev. Mater.* **1** 16055

[14] Rycerz A, Tworzydło J and Beenakker C W J 2007 *Nat. Phys.* **3** 172

[15] Xiao D, Yao W and Niu Q 2007 *Phys. Rev. Lett.* **99** 236809

[16] Xiao D, Liu G B, Feng W, Xu X and Yao W 2012 *Phys. Rev. Lett.* **108** 196802

[17] Mak K F, McGill K L, Park J and McEuen P L 2014 *Science* **344** 1489

[18] Aivazian G, Gong Z, Jones A M, Chu R L, Yan J, Mandrus D G, Zhang C, Cobden D, Yao W and Xu X 2015 *Nat. Phys.* **11** 148

[19] Srivastava A, Sidler M, Allain A V, Lembke D S, Kis A and Imamoğlu A 2015 *Nat. Phys.* **11** 141

[20] Li Y, Ludwig J, Low T, Chernikov A, Cui X, Arefe G, Kim Y D, van der Zande A M, Rigosi A, Hill H M, Kim S H, Hone J, Li Z, Smirnov D and Heinz T F 2014 *Phys. Rev. Lett.* **113** 266804

[21] Guo S D, Guo X S and Wang G 2024 *Phys. Rev. B* **110** 184408

[22] Tan C Y, Gao Z F, Yang H C, Liu Z X, Liu K, Guo P J and Lu Z Y 2025 *Phys. Rev. B* **111** 094411

[23] Xie W, Wang L, Xu X, Yue Y, Xia H, He L and Wang H 2025 *Acta Phys. Sin.* **74** 227502 (in Chinese)

[24] Guo S D 2025 *Appl. Phys. Lett.* **126** 080502

[25] She Y, Wang Y, Sun H, Wu C, Zhang W and Li P 2026 *Phys. Rev. B* **113** 035420

[26] Zhang X and Zhang S 2026 *Front. Phys.* **21** 075203

[27] Wang Q, Wu D W, Guo G H, Long M Q and Wang Y P 2024 *Chin. Phys. B* **33** 097507

[28] Li J Y, Fan A D, Wang Y K, Zhang Y and Li S 2024 *Appl. Phys. Lett.* **125** 222404

[29] Zhang W, Zhu E, Li Z and Lv H 2025 *Phys. Rev. B* **112** 144427

[30] Xie W, Xu X, Yue Y, Xia H and Wang H 2025 *Phys. Rev. B* **111** 134429

[31] Jiang Y, Zhang X, Bai H, Tian Y, Zhang B, Gong W J and Kong X 2025 *Appl. Phys. Lett.* **126** 053102

[32] Zhu Y, Chen T, Li Y, Qiao L, Ma X, Liu C, Hu T, Gao H and Ren W 2024 *Nano Lett.* **24** 472

[33] Hu X, Zhao W, Xia W, Sun H, Wu C, Wu Y Z and Li P 2025 *Appl. Phys. Lett.* **127** 011905

[34] Chen C, He X, Xiong Q, Quan C, Hou H, Ji S, Yang J and Li X 2025 *Appl. Phys. Lett.* **127** 102409

[35] Khan I, Bezzerga D, Marfoua B and Hong J 2025 *npj 2D Mater. Appl.* **9** 18

[36] Guo S D, Guo X S, Cheng K, Wang K and Ang Y S 2023 *Appl. Phys. Lett.* **123** 082401

[37] Ma Q, Wang B, Yang G and Liu Y 2025 *Appl. Phys. Lett.* **126** 223106

[38] Kresse G and Furthmüller J 1996 *Comput. Mater. Sci.* **6** 15

[39] Kresse G and Furthmüller J 1996 *Phys. Rev. B* **54** 11169

[40] Blöchl P E 1994 *Phys. Rev. B* **50** 17953

[41] Perdew J P, Burke K and Ernzerhof M 1996 *Phys. Rev. Lett.* **77** 3865

[42] Anisimov V I, Zaanen J and Andersen O K 1991 *Phys. Rev. B* **44** 943

[43] Dudarev S L, Botton G A, Savrasov S Y, Humphreys C J and Sutton A P 1998 *Phys. Rev. B* **57** 1505

[44] Moore G C, Horton M K, Linscott E, Ganose A M, Siron M, O'Regan D D and Persson K A 2024 *Phys. Rev. Mater.* **8** 014409

[45] Togo A and Tanaka I 2015 *Scr. Mater.* **108** 1

[46] Nosé S 1984 *J. Chem. Phys.* **81** 511

[47] Marzari N, Mostofi A A, Yates J R, Souza I and Vanderbilt D 2012 *Rev. Mod. Phys.* **84** 1419

[48] Mostofi A A, Yates J R, Pizzi G, Lee Y S, Souza I, Vanderbilt D and Marzari N 2014 *Comput. Phys. Commun.* **185** 2309

[49] Xu R, Gao Y and Liu J 2026 *Natl. Sci. Rev.* **13** nwaf528